Review of Scientific Instruments ARTICLE pubs.aip.org/aip/rsi

A configurable two-tone electron spin resonance spectrometer

Cite as: Rev. Sci. Instrum. 95, 124710 (2024); doi: 10.1063/5.0231566
Submitted: 31 July 2024 • Accepted: 4 December 2024 •
Published Online: 26 December 2024

Charles A. Collett,[1,a)] Sofia M. Davvetas,[2] Abdulelah Alsuhaymi,[3] and Grigore A. Timco[3]

AFFILIATIONS

[1] Department of Physics, Hamilton College, Clinton, New York 13323, USA
[2] Department of Physics, Muhlenberg College, Allentown, Pennsylvania 18104, USA
[3] School of Chemistry, The University of Manchester, Manchester M13 9PL, United Kingdom

[a)] **Author to whom correspondence should be addressed:** cacollet@hamilton.edu

ABSTRACT

Electron spin resonance (ESR) is a powerful tool for characterizing and manipulating spin systems, but commercial ESR spectrometers can be inflexible and designed to work in narrow frequency bands. This work presents a spectrometer built from off-the-shelf parts that, when coupled with easy-to-design resonators, enables ESR over a broad frequency range, including at frequencies outside the standard bands. It can operate at either a single frequency or at two frequencies simultaneously. The spectrometer is controlled by a field programmable gate array (FPGA), and new capabilities can be easily added by reconfiguring the FPGA and adding or swapping components. We demonstrate the capabilities of the spectrometer using the molecular nanomagnet Cr_7Mn, including simultaneous ESR at frequencies separated by nearly 500 MHz.

I. INTRODUCTION

Electron spin systems are a subject of significant interest for the possibility of forming spin qubits.[1–3] One of the main ways of manipulating and reading out the states of these spins is electron spin resonance (ESR), where radio-frequency (RF) voltage signals are transduced into oscillating magnetic fields that interact with the spins.[4] The response of the spins to these RF excitations is then detected, with the signal generation and detection being performed by an ESR spectrometer.[5] This work presents an ESR spectrometer that is both flexible and made from off-the-shelf components, making it possible to precisely tune to spins across a wide frequency range from ~2 to 15 GHz, either at a single frequency in monochromatic mode or simultaneously at any two frequencies in that range in two-tone mode.

As currently configured, our spectrometer addresses the 2–6 GHz range, needing only to change the RF circulator to swap between 2–4 GHz and 4–6 GHz, but minor adjustments laid out in Appendix B can allow it to address the 6–15 GHz range. It is also possible to address multiple ranges simultaneously by using different components in two-tone mode as described below. Our spectrometer excites spin samples by coupling a signal generator, able to produce sinusoidal voltages at a variety of frequencies and powers, with a resonator, which converts the voltage into an oscillating magnetic field applied to the spin sample. Any signal from the sample itself is detected using the same resonator, then down-converted using an IQ mixer for readout on an oscilloscope. Overall control is provided by a field-programmable gate array (FPGA).

In recent years, it has become much easier and more affordable to design ESR spectrometers by coupling high-frequency FPGAs with digital-to-analog converters (DACs) for signal generation and analog-to-digital converters (ADCs) for detection.[6–10] Such designs offer many benefits, including very granular control over the frequency and amplitude of the produced signals. However, their frequency ranges can be somewhat limited by the sampling rate of the electronics, with, for instance, a 5 GSample/s (GSPS) converter needing to work in Nyquist zone 3 to generate a 6 GHz signal,[11] potentially resulting in a reduction in power and the presence of unwanted sidebands. By trading the granular control for a simpler design using off-the-shelf components, we have developed a spectrometer that has only very rudimentary signal shaping capabilities, mostly constrained to square pulses of varying powers, but that can work at much higher frequencies just by swapping out components to match the desired range. The relative simplicity of the

spectrometer also makes it fairly straightforward to configure and extend its functionality and to understand how each part of the spectrometer works.

We developed this spectrometer in part to allow for both individual and simultaneous control and readout of the spins in a dimer of molecular nanomagnets (MNMs). MNMs are a class of magnetic materials allowing for chemical engineering of the properties of the quantum spins, with potential quantum computing applications using the molecules as spin qubits.[3,12,13] Performing multi-qubit gates with MNMs will involve simultaneous ESR on multiple spin qubits with frequencies separated by multiple GHz.[14] Our lab has recently focused on MNMs engineered to have atomic clock transitions,[15] which extend the quantum state lifetime T_2 by making the spins less sensitive to local field fluctuations. Dimers of these MNMs can be used to perform quantum gates,[16] but only with a spectrometer that can drive each spin simultaneously, and our spectrometer makes this possible.

Below we describe in detail the composition and performance of our spectrometer. Most of the components are commercially available, and we will only briefly discuss their role; a more general discussion of spectrometer design can be found elsewhere.[4,5]

II. SPECTROMETER DESIGN

Using the configuration presented in this work, the spectrometer can produce pulses as short as 20 ns and up to 22 dBm (150 mW) of power at the output to the resonator. It can switch between continuous-wave (CW) and pulsed signals programmatically, though CW mode is mostly useful for doing preliminary characterization of resonator frequencies, as more sensitive and precise CW measurements can be performed with a vector network analyzer. Our main goal in developing this spectrometer is to perform pulsed experiments, and as such, only pulsed signals and results are presented here.

The design of this spectrometer can be broken down into three parts: the source and detection electronics, the resonator portion that directly interacts with the spins, and the FPGA controller.

A. Electronics

Figure 1 shows a circuit diagram of the spectrometer electronics in both monochromatic and two-tone configurations; in monochromatic mode, all pink lines and components are omitted. Details of the exact off-the-shelf components used can be found in Appendix A.

1. Monochromatic source

An RF source generates one or two CW output signals at a single RF frequency (the carrier frequency ν_c), which is our excitation and detection frequency. One of these signals, which we will label B, goes directly into a high-speed RF switch ("pulse switch," PS_B in Fig. 1), while signal A goes through a power divider (PD), with half of the power going to the detection mixer (see below) and the other half to its own pulse switch (PS_A). Pulsed experiments generally use both outputs to exploit the coherent phase control between the two signals that our source enables, which we will discuss later. The pulse switches are controlled by the FPGA, opening and closing as needed to generate either CW or pulsed outputs. The signal from both switches is combined in a power combiner

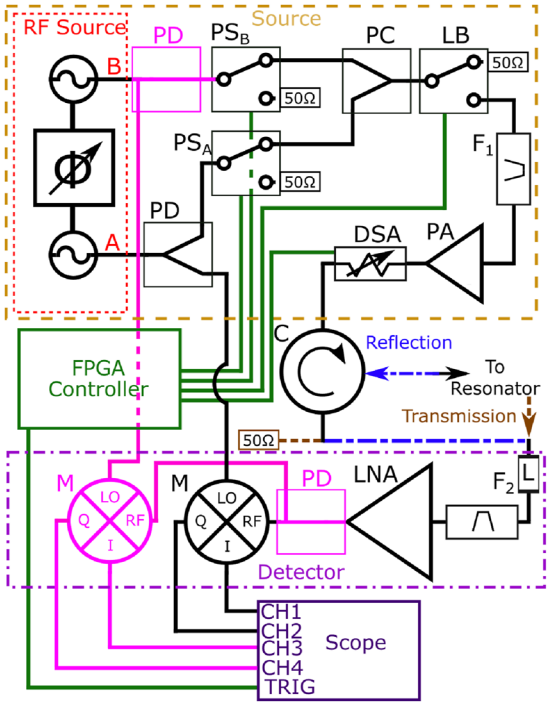

FIG. 1. A circuit diagram showing the layout and connections of the spectrometer in both monochromatic and two-tone configurations. Component labels are referenced in the text. Pink lines and components are associated with the two-tone configuration and are omitted in the monochromatic configuration. Blue dashed–dotted lines near the circulator C indicate the reflection mode configuration, while brown dashed lines indicate transmission mode; in either mode, the lines associated with the other mode are omitted.

(PC, which is a reversed power divider) and optionally put through a bandpass filter (F_1) to reduce noise. We found that even with the pulse switches open, there is still enough of the carrier signal leaking through to be detected, so the signal then goes through a blocking switch (LB, for Leakage Block) to more completely attenuate that leaking signal. This combined signal is then sent through a power amplifier (PA) and a digital step attenuator (DSA). The DSA is controlled by the FPGA and allows independent control of the power of each pulse and potentially shaping the power within a single pulse (that capability is not implemented in the default configuration). Finally, the signal is routed to an antenna coupled to the resonator through a circulator (C) to prevent reflected power from damaging the amplifier.

The spectrometer can work in reflection mode when a single antenna is coupled to the resonator and both reflection and transmission mode with two antennas. In reflection mode, shown as the blue dashed–dotted lines in Fig. 1, after the signal has interacted with the resonator, it travels back up the same coaxial cable to the circulator, which routes it to the detection electronics. In transmission mode, shown as the brown dashed lines, the third output from the circulator is capped with a 50 Ω terminator, and a coaxial cable attached to the second antenna brings any transmitted signal to the detection electronics.

2. Monochromatic detection

The returning signal first passes through a power limiter (L) to protect the detection circuitry from the initial high-power pulses. This protection could also be achieved using another switch, and indeed both configurations have been tested with similar results, but the limiter, being a passive component, is simpler. We have found that under normal operating conditions there will often not be enough power reaching the detection side to require the limiter, but we leave it in for convenience and safety, as it causes minimal loss (<0.6 dB at these frequencies).

The remaining signal optionally passes through another band-pass filter (F_2) and then enters a low-noise amplifier (LNA). At this point, the signal is an RF voltage that has been modified in some way by interactions with the resonator and sample. Note that while we output only one frequency, the return signal may have several due to those interactions. It is possible to directly detect signals at these other frequencies by exciting at one frequency and detecting at another, but for this work, we will focus on homodyne detection of the signal oscillating at ν_c. The amplified return signal goes into the RF port of an IQ mixer (M), and with the carrier frequency coming into its LO port, the mixer downconverts the signal into low-frequency in-phase (I) and quadrature (Q) signals, which can then be read out on an oscilloscope (Scope).

3. Two-tone electronics

We create two-tone pulses with two different output frequencies, ν_A and ν_B, by simply changing the frequency of one of the RF source outputs. With the exact same electronics, this only provides a two-tone source, as with the monochromatic configuration, detection is still only possible at ν_A. To also do two-tone detection, fairly minor changes need to be made to the electronics, adding a power divider and a mixer to output B to match those on output A, and then dividing the returning signal after the LNA to send it to the RF ports of both mixers; these changes are shown in pink in Fig. 1. Note that in this case the spectrometer is doing homodyne detection for both frequencies, though if the frequencies are too close together there will be some crosstalk.

If desired, either or both the source or detection electronics can be more comprehensively separated to provide more independent two-tone functionality. For instance, putting in pulses at different frequencies and different powers would require at least separate DSAs, and maximizing the pulse and signal size at each frequency could be performed by using two separate antennas, both coupled to the resonator, so each frequency gets dedicated power and low-noise amplifiers. The preliminary two-tone results presented below use the simpler changes described earlier.

B. Resonator

As discussed earlier, the resonator must be able to couple the spins to an oscillating magnetic field. For this spectrometer, samples are placed into the loop of a loop-gap resonator (LGR).[17–19] This style of resonator is formed by shaping a conductor into a connected loop and gap, such that current must flow around the loop to get from one side of the gap to the other. The resonator can thus be modeled as a lumped-element RLC circuit with resonant frequency ν_r, with the loop forming the inductor, the gap the capacitor, and the copper body the resistor. This design concentrates the oscillating magnetic field inside the loop; the loop dimensions (mm-scale) are generally much smaller than the RF wavelength (cm-scale for GHz frequencies), such that there is a high filling factor for a sample placed in the loop. With this design, a relatively low input power translates into a sizable magnetic field strength at the sample, and a small oscillating field from the sample can more easily couple back into the resonator.

Two resonators are used in this work, a monomodal LGR that resonates at a single frequency and a bimodal LGR that resonates at two frequencies simultaneously to enable ESR at widely separated frequencies. Both are made from 1/8 in. (0.3175 cm) thick OFHC copper and have mounting holes on the sides for 0–80 screws. The monomodal resonator, shown in Fig. 2(a), is a single-loop–single-gap design made out of a disk 0.6 in. (1.524 cm) in diameter with a 0.06 in. (0.152 cm) diameter loop and a gap 0.03 in. (0.076 cm) wide and 0.394 in. (1.000 cm) long milled out of it. The bimodal resonator, shown in Fig. 2(b), is constructed from two single-loop–single-gap designs machined perpendicularly into the same piece of copper, with tabs on the sides for the mounting holes. The main body of the LGR is 0.24 in. (0.610 cm) wide and 0.6 in. (1.524 cm) long. Both loops are 0.06 in. (0.152 cm) in diameter, and both gaps are 0.040 in. (0.102 cm) wide and 0.480 in. (1.219 cm) long. The key feature of this design is that the loops form a cross, so a sample placed in the center of the cross will experience the oscillating fields from both loops, which will resonate at different frequencies. Design files for both resonators are provided in the supplementary material.

To interact with the sample, the resonator must transduce an oscillating voltage into an oscillating loop field. The voltage is introduced to the resonator via an antenna formed from the exposed inner conductor at the end of a coaxial cable, which is placed near the surface of the resonator. A capacitive antenna is made by bending the exposed inner conductor into an "L" shape, then lowering it near the gap, while an inductive antenna sits over the loop and is made by making a circle with the inner conductor and electrically connecting it to the outer conductor. The resonator is attached with nylon screws and washers to a copper RF shield at the bottom of a sample probe that is inserted into a cryostat, and coaxial cables transmit signals between the rest of the spectrometer and the resonator through

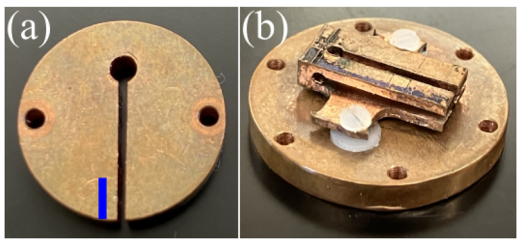

FIG. 2. The loop-gap resonators used for this work, (a) a monomodal design with a single loop and gap and (b) a bimodal design featuring two crossed loops and gaps. (b) also shows the resonator mounted to the bottom of the RF shield with 0–80 nylon screws and washers. Resonator specifications are given in the text. The blue rectangle overlaid on (a) indicates the approximate position of the capacitive antenna used in this work.

one or more antennas inside the shield. In reflection mode, a single antenna serves to both excite the resonator and detect signals coming from the sample, and in transmission mode, one antenna does the excitation and a different antenna does the detection. Transmission mode thus requires two sets of antennas and coaxial cables in the sample probe, which can be terminated if unused.

A detailed description of a substantially similar antenna–resonator arrangement can be found in Ref. 20, with the only significant variations for the work described here being the antenna length and placement. For both resonators, we used a capacitive antenna, removing ~3 mm of outer conductor and dielectric from a 0.086 in. (0.218 cm) diameter copper coaxial cable and bending the exposed inner conductor 90° directly beneath the remaining outer conductor. The antenna was placed over the copper on one side of the resonator, ~1 mm from the edge of the gap with the tip of the "L" approximately flush with the edge of the resonator, as depicted by the blue rectangle overlaid on Fig. 2(a) (a similar position was chosen for the bimodal resonator). It was oriented parallel to the gap so the "L" pointed away from the loop and lowered close to the surface of the resonator to provide antenna–resonator coupling. We found that this single antenna was sufficient to interact with both resonances of our bimodal resonator, and that slight changes in its distance to the gap or to the edge of the resonator did not significantly affect the coupling for either resonator.

The resonators are characterized by both ν_r and the width of their resonance peaks $\Delta\nu_r$. These values combine to give the quality factor of the resonator,

$$Q = \frac{\nu_r}{\Delta\nu_r}. \tag{1}$$

The monomodal resonator used in this work has a room-temperature resonant frequency of $\nu \sim 3.98$ GHz and an unloaded Q of ~170, and at 3 K, as characterized below, $\nu \sim 3.902$ GHz and $Q \sim 200$. This low Q is good for pulsed experiments as the pulse shape is less distorted with lower Q values. The bimodal resonator used in this work has room-temperature resonant frequencies of $\nu_A \sim 3.99$ GHz and $\nu_B \sim 4.48$ GHz, with unloaded Q's of ~160 and ~130, respectively. At 3 K, the frequencies are $\nu_A \sim 4.02$ GHz and $\nu_B \sim 4.49$ GHz, with $Q_A \sim 350$ and $Q_B \sim 380$, allowing simultaneous ESR at frequencies separated by $\Delta\nu \sim 470$ MHz. Significantly larger frequency separations can be achieved by changing the bimodal design parameters.

Another important figure of merit for resonators is their conversion factor,

$$c = \frac{B_1}{\sqrt{QP}}, \tag{2}$$

where B_1 is the RF field strength and P is the input power. The field strength can be estimated from the pulse width required to generate a given spin tip angle β using the relationship $\beta = g\mu_B B_1 t_p$, where g is the g-factor of the spin sample (for our spin samples, $g = 1.96$;[21] see below). Based on the pulse lengths required to generate π spin rotations for each resonator (110 ns for the monomodal and 100 ns for both resonances of the bimodal, as discussed below), we can roughly estimate the B_1 field strengths generated in each to be $B_1 \sim 10$ G. With the Q values reported above and our input power of 21 dBm, this corresponds to a conversion factor of $c \sim 2\,\mathrm{G}/\sqrt{\mathrm{W}}$ for both resonators.

C. Controller

Aside from the RF source, most of the components described earlier are "dumb," in that they do not require any control input telling them what to do; they just perform their assigned task with whatever signal inputs they get. There are three significant "smart" exceptions that take TTL inputs: the switches have control inputs that open and close them; the digital step attenuator has an input that controls the attenuation of the signal; and the oscilloscope has a trigger input. All of these control inputs are provided by a low-cost FPGA running a custom configuration written in the hardware description language Verilog. For the FPGAs targeted in this work, the control logic can be simulated and verified using open-source tools, enabling fast iteration and development. As currently configured, the FPGA runs at 200 MHz, setting a minimum timestep of 5 ns for any of the control inputs. The frequency is configurable, and this frequency was chosen to minimize the timestep while ensuring stable operation of the control program, as running it any faster could create situations where signals propagating within the FPGA would not be able to reach their destinations in time for the next clock tick, introducing random deviations from the programmed behavior.

Using an FPGA in this way provides a great deal of expandability for the spectrometer. Adding additional "smart" components, or the ability to create more complex pulse sequences, can be performed by writing additional control logic into the Verilog configuration. Such expansion would likely require the reduction of the clock speed, but increasing the timestep to 10 ns, for example, would allow for a significant amount of expansion, such as the addition of more pulses to perform Carr–Purcell–Meiboom–Gill sequences.[22]

The initial configuration of the FPGA is performed by writing out the control logic in Verilog and loading it onto the board. All code used to configure and interact with the FPGA is provided in the supplementary material. As currently configured, the FPGA supports up to two independent RF output channels, either in CW mode (with one or the other output enabled at any given time) or in pulsed mode with up to three independent pulses on one output channel and up to two independent pulses on the other. While fully reconfiguring the FPGA takes tens of seconds, a variety of the control parameters are directly adjustable via USB at a fraction of that time. These parameters will be highlighted when they are introduced in Sec. III B.

III. SPECTROMETER OPERATION

This section will focus on the important operational details of our spectrometer and will not cover the basics of ESR operation; for a more general overview of both CW and pulsed ESR, see Refs. 5 and 23. The general procedure is to find the resonant frequency of the resonator and then perform one or more pulsed experiments to manipulate and probe the spin sample.

Characterization was performed at zero applied magnetic field using the resonators described above in two separate cooldowns, coupled to a capacitive antenna in reflection mode with an input power of 21 dBm, while immersed in a bath of liquid helium at

3.0 K in a Janis SHI-950T cryostat. The samples used for these experiments were two variants of the MNM Cr_7Mn,[21,24] both diluted by volume in toluene. For the monochromatic experiments, we used a 10% solution of $[Pr_2NH_2][Cr_7MnF_8(Piv)_{15}(O_2C\text{-}py]$ (**A**), and for the two-tone experiments, we used a 5% solution of $[Et_2NH_2][Cr_7\ MnF_8(Piv)_{16}]$ (**B**). These samples were chosen based on their zero-field clock transitions around 4 GHz, our familiarity with them from previous work,[15] and because future work will explore using dimers of this MNM as spin qubits.[16] Sample **B** has significant inhomogeneous broadening, allowing echoes to be detected at zero field over a frequency range from below 4 GHz to above 5 GHz, while sample **A** has significantly less broadening and, therefore, a much narrower but stronger signal around 3.95 GHz. All the data presented here were taken on a 4-channel Tektronix MSO24 2-BW-70 oscilloscope; monochromatic experiments can be performed with a two-channel oscilloscope (we have used a Tektronix TBS1052C with equivalent results), but two-tone experiments require either one four-channel scope or two two-channel scopes.

A. Determining ν_r

As previously mentioned, the current version of this spectrometer uses CW ESR only for preliminary resonator characterization, letting us scan the input frequency for dips in the background associated with the resonant frequency ν_r. Precisely determining ν_r is performed by sending in a short (~50 ns) pulse at ν_c and monitoring the response immediately after it ends. When ν_c is far from ν_r, there will be effectively no signal. However, when ν_c is at or near ν_r, the resonator will absorb energy from the pulse, and when the pulse ends, that energy will radiate back into the antenna over a decay time,

$$t_{\text{decay}} = \frac{Q}{\pi \nu_r}. \tag{3}$$

That produces a "ring-down" signal near ν_r; Fig. 3(a) shows the in-phase (I) portion of such a signal for the monomodal resonator used in this work at 3 K, and Fig. 3(c) shows the amplitude of the same signal, calculated from the in-phase (V_I) and quadrature voltages (V_Q) as

$$V_{\text{Amp}} = \sqrt{V_I^2 + V_Q^2}. \tag{4}$$

Finding ν_r from these data can be performed in two ways. The first takes a fixed-time cut of the amplitude data and fits the square of that voltage (to get a quantity proportional to power) vs the carrier frequency to a Lorentzian function, giving the central frequency ν_r and the width of the peak $\Delta\nu_r$. An example of this for the monomodal resonator is shown in Fig. 3(d), for the vertical cut indicated by the yellow dashed line in (c) at 178 ns, yielding $\nu_r = 3902.0 \pm 0.3$ MHz (indicated by the black horizontal line) and $\Delta\nu_r = 19.1 \pm 0.8$ MHz (indicated by the vertical green line). The second method uses the oscillations that are present in either the I or Q signals, as seen in Fig. 3(a). Applying a carrier frequency ν_c that is detuned from the resonator frequency ν_r results in a time-dependent phase shift, oscillating the signal between I and Q at the beat frequency $\nu_b = |\nu_c - \nu_r|$. Taking the Fourier transform of the I or Q data, as shown in Fig. 3(b), allows the extraction of that beat frequency as a function of ν_c, and fitting those data to find where it goes to zero

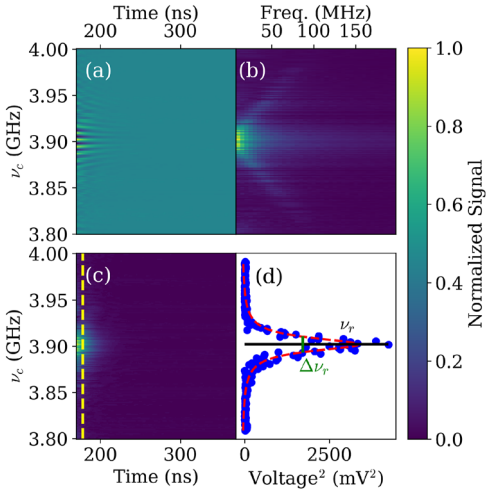

FIG. 3. Monomodal resonator frequency sweep data taken at 3 K. (a) Reflected in-phase signal V_I from the resonator showing the ring-down and beating near ν_r. (b) Fourier transform of the signal from (a), showing the weight of different frequencies in the reflected signal shifting as ν_c is detuned from ν_r. The maximum Fourier weight occurs at the beat frequency $\nu_b = |\nu_c - \nu_r|$. (c) Reflected amplitude signal V_{Amp}. (d) Vertical cut of amplitude signal from (c) taken at 178 ns, along the dashed yellow line, then squared. The red dashed line is a Lorentzian fit, yielding $\nu_r = 3.902$ GHz and $\Delta\nu_r = 19$ MHz.

gives ν_r. Once ν_r is found by either method, the quality factor Q can be found using Eq. (1) with the results of the Lorentzian fit or by simply fitting the ring-down signal at ν_r to a decaying exponential and plugging the resulting time constant and frequency into Eq. (3). As shown below, we found that our ν_r results were generally equivalent with either method, but that the exponential fit gave a more precise measurement of Q. For the monomodal resonator used in this work, the Lorentzian and Fourier methods give 3 K resonant frequencies of $\nu_r = 3902.0 \pm 0.3$ and $\nu_r = 3901.9 \pm 0.3$ MHz, respectively, and the quality factor is $Q = 198 \pm 1$ from the exponential fit and $Q = 204 \pm 9$ from the Lorentzian fit. For the bimodal resonator at 3 K, we found $\nu_A = 4023.8 \pm 0.2$ MHz and $\nu_B = 4488.2 \pm 0.2$ MHz using the Lorentzian method, and $Q_A = 346 \pm 3$ and $Q_B = 377 \pm 2$ using the exponential fit.

B. Pulse generation

Once ν_r is determined, a variety of spin echo experiments can be performed by generating one or more sets of pulses, depending on whether the spectrometer is operating at a single frequency on one or two outputs (monochromatic) or at two different frequencies for the two outputs (two-tone).

1. Monochromatic pulses

As noted earlier, the spectrometer can create up to three pulses at a single frequency, using either one or both outputs; the third pulse is currently only enabled on output *B*. The default configuration has two of the pulses forming a Hahn echo pulse sequence, the first having a width of $t_{\pi/2}$ and the second a width of t_π, with a delay τ between them. The third pulse is optionally used as a nutation pulse, occurring an amount of time τ_{nut} before the first Hahn

pulse and having a width of t_{nut}. As currently configured, all pulses are programmatically adjustable in increments of the timestep, 5 ns, with a minimum value of 20 ns and a maximum value of 327.68 μs, with the exception of t_{nut}, which has a maximum value of 1.28 μs; the 20 ns minimum pulse time is set by the on/off time of our switches. The delays between any of the pulses are adjustable from 5 ns to 327.68 μs, and the sequence repetition time T is adjustable from 5 ns to 21.47 s. The first Hahn pulse is also attenuated by 3 dB relative to the other pulses, giving it half the power so that the width of the two Hahn pulses can be the same. The scope trigger rising edge is coincident with the rising edge of the first Hahn pulse; the included acquisition code is configured to trigger the scope on the rising edge and automatically offset to put the expected echo on the scope screen.

2. Two-tone pulses

The two RF outputs can also produce two different frequencies, either for two-tone ESR or for heterodyne detection. As discussed in the two-tone electronics section (Sec. II A 3), minor changes to the electronics are required for simultaneous detection at both frequencies. The spectrometer can create one or two pulses for each output, and as with the monochromatic setup, output B can also have a third pulse. The details are mostly the same as with the monochromatic pulses, and the extra attenuation is timed to coincide with the first Hahn pulse on output A. It is trivial to swap the frequencies of each output.

C. Background subtraction

Once ν_r is determined, a Hahn echo sequence is performed. If there is a strong enough echo signal over the desired experimental parameters, experiments can be performed directly by integrating the signal over an appropriate range. Unfortunately, for many situations, the signal-to-noise ratio is too low for this to be an effective approach, due to a variety of factors, including small samples and large amounts of background noise. To address these issues, we have two main tools: averaging over multiple signals and background subtraction. The oscilloscope has built-in averaging, but it is often necessary to take more averages than the maximum provided by the scope. Our acquisition software in the supplementary material enables additional averaging as needed, with no upper limit (the functional upper limit is the amount of time required).

If white noise is the only factor making it difficult to see the signal, averaging can suffice to bring out the signal. However, there can also be systematic offsets coming from the other electronics for a variety of reasons, and averaging will not remove these. Instead, we combine averaging with background subtraction, where we take two different measurements where ideally the only thing that changes is the spin echo signal, and then subtract one from the other to remove a variety of non-sample-dependent background effects, such as ground fluctuations when the RF switches open and close, or cavity ring-down. We do this either by changing the Hahn echo delay τ or by changing the relative phase between outputs A and B. Not all backgrounds can be removed with these methods, but they have proved quite effective at removing a range of electronic artifacts that would otherwise obscure the spin echo signal; because the resonator ring-down depends on the phase of the input signal, it can only be subtracted using the delay-based method. For our background subtraction comparison, shown in Fig. 4, we chose τ such that the background includes some resonator ring-down. Note that delay-based subtraction can be performed with any configuration of the spectrometer, but phase-cycling requires a monochromatic experiment with output A providing the reference frequency (going into the LO port of the mixer) and output B providing the excitation pulses. Phase-cycling generally results in a higher signal-to-noise ratio when the background is not phase-dependent.

For our delay-based background subtraction, we set up our Hahn echo sequence and take a signal measurement V_{sig}, as shown by the blue squares in Fig. 4(a). We then change τ (increasing it by 5 μs if $\tau < 10$ μs, otherwise decreasing it by 5 μs) but keep the scope window fixed to shift the expected echo signal out of the scope window while leaving the background mostly unchanged and take a background measurement V_{back} as shown by the orange triangles in Fig. 4(a). Subtracting V_{back} from V_{sig} gives us our data, $V_{data} = V_{sig} - V_{back}$, as shown by the green circles in Fig. 4(a), where the resonator ring-down background has been mostly removed.

For our phase-cycled background subtraction, we exploit the fact that if we shift the phase of an input signal by $\Delta\phi = 180°$, the portion of the output signal that was downconverted from the carrier frequency (and, therefore, was coming from the resonator and sample) will be inverted. With our Hahn echo sequence set up and with a relative phase of $\Delta\phi = 0$, we can take an in-phase measurement V_0, as shown by the blue squares in Fig. 4(b). If we then change the relative phase to $\Delta\phi = 180°$, we can take an inverted measurement V_{180}, as shown by the orange triangles in Fig. 4(b). The low-frequency background in each measurement will be largely identical, because

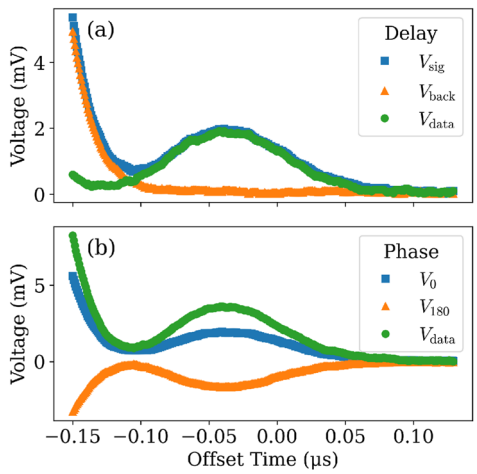

FIG. 4. Comparison of our two methods for background subtraction at 3 K using the monomodal resonator at $\nu_r = 3.902$ GHz, based on a Hahn echo sequence with 70 ns pulse widths and inter-pulse delay $\tau = 150$ ns to include some of the resonator ring-down. Methods are described in the main text. (a) Delay-based background subtraction, with signal trace V_{sig} shown as blue squares, background trace V_{back} as orange triangles, and background-subtracted data $V_{data} = V_{sig} - V_{back}$ as green circles. (b) Phase-cycling background subtraction, with $\Delta\phi = 0$ (V_0) shown as blue squares, $\Delta\phi = 180°$ (V_{180}) as orange triangles, and background-subtracted data $V_{data} = V_0 - V_{180}$ as green circles. This removes some portion of the background and doubles the height of the echo.

much of it does not depend on the phase, but the echo signal will now be inverted; as noted above, one background that does depend on the phase is resonator ring-down, so if that significantly contributes to the background in an experiment, the delay-based background subtraction should be used. If we then take $V_{\text{data}} = V_{180} - V_0$, we will be subtracting the background but doubling the echo signal, as shown by the green circles in Fig. 4(b); these data are usually halved to maintain a constant signal size. The resonator ring-down background, being phase-dependent, is still present.

D. Standard experiments

While many different experiments can be made with the spectrometer as currently configured, here we present several that are included as turn-key options in the acquisition code. Many other experiments using 1–5 pulses can be set up with minor changes to the acquisition code, and experiments using more pulses can be implemented by changing the FPGA configuration. For each experiment, phase-cycling was used for background subtraction, with delay times τ chosen to exclude any resonator ring-down from the background.

1. Monochromatic experiments

Three different single-frequency experiments are shown in Fig. 5. In addition to these experiments, the acquisition software is also configured to easily do pulse sweep measurements (sweeping $t_{\pi/2}$ and t_π), phase sweep measurements (sweeping $\Delta\phi$), and frequency sweep measurements (sweeping ν_c).

In (a), we present a Rabi oscillation experiment. A Hahn echo pulse sequence is set up with $t_{\pi/2} = t_\pi = 110$ ns (based on a rough preliminary sweep of the pulse widths) and $\tau = 250$ ns. A nutation pulse is sent 5 μs before the $\pi/2$ pulse, and the width of the nutation pulse t_{nut} is swept from 0 to 400 ns. Integrating the area under the echo results in the data shown in Fig. 5(d), and fitting those data to a decaying sinusoid (the green dashed line) returns a $\pi/2$ pulse time of 106 ± 2 ns.

In (b), we present an inversion recovery experiment. $t_{\pi/2}$ and t_π are both set to the 110 ns pulse width determined in the Rabi experiment, with the same τ as in (a), and a nutation pulse of width $t_{\text{nut}} = 110$ ns; because the attenuator only adds attenuation to the $\pi/2$ pulse, this nutation pulse performs a π rotation. The delay between the nutation pulse and the $\pi/2$ pulse, T, is swept from 5 to 100 μs to determine the longitudinal relaxation rate T_1. Fitting the integrated echo to an exponential [as shown in Fig. 5(e)] yields $T_1 = 23 \pm 1$ μs.

Finally, in (c), we present a Hahn echo delay sweep. The same Hahn echo pulse times from (b) are used, but now τ is swept from 250 to 1500 ns to determine the transverse relaxation rate T_2. Figure 5(f) shows the integrated echo data and an exponential fit that yields $T_2 = 390 \pm 10$ ns (this value is limited by our temperature and level of dilution).

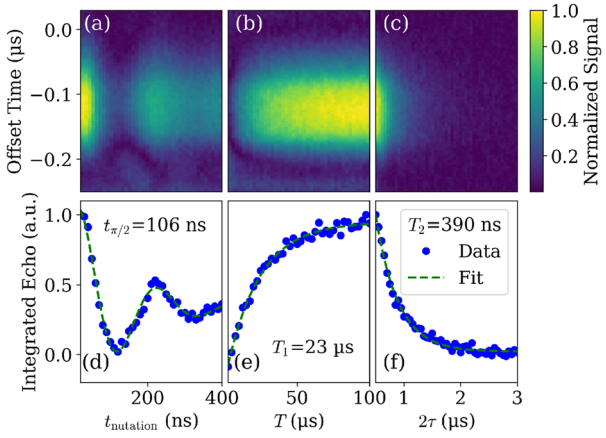

FIG. 5. Characterization of monochromatic spin echo experiments on sample **A** at 3 K using the monomodal resonator at $\nu_r = 3.902$ GHz. All data are phase-cycled. In all lower panels, integrated echo area is shown as blue circles, while appropriate fits to the echo area are shown as dashed green lines. Data (a) and fitted echo area (d) for a Rabi oscillation experiment, sweeping the nutation pulse width t_{nut} to find the appropriate $\pi/2$ pulse width $t_{\pi/2}$. Data (b) and fitted echo area (e) for an inversion recovery experiment, sweeping the delay T between an inverting nutation pulse and the $\pi/2$ pulse to measure T_1. Data (c) and fitted echo area (f) for a Hahn echo delay sweep, sweeping the inter-pulse delay τ to measure T_2.

2. Two-tone experiments

With two separate output frequencies, all of the monochromatic experiments can be performed on each frequency individually (with the exception of the phase sweep), but it is also possible to

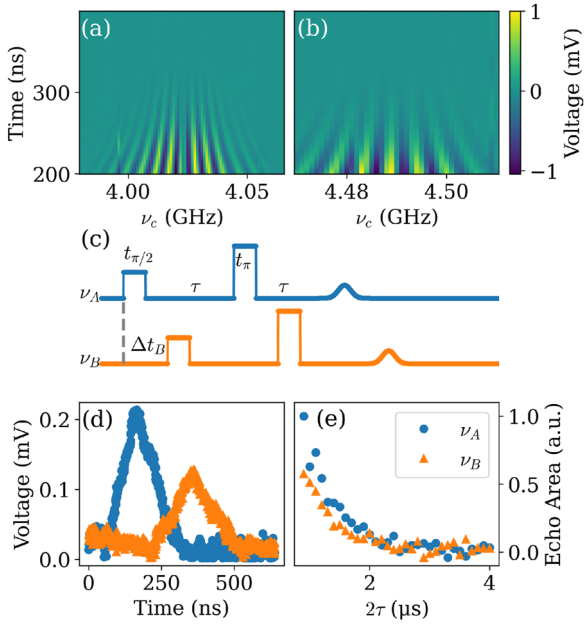

FIG. 6. Demonstration of a simultaneous two-tone Hahn echo delay sweep experiment on sample **B** at 3 K using the bimodal resonator. Frequency sweep data for the lower (a) and higher (b) frequency resonances of the resonator, yielding $\nu_A = 4024$ MHz and $\nu_B = 4488$ MHz. (c) Pulse sequence schematic for this simultaneous Hahn echo experiment, using identical pulse widths and delay times, but with an overall time offset Δt_B for the higher frequency. (d) Background-subtracted echo signal at each frequency, with the signal at ν_A (blue circles) occurring a time Δt_B before the signal at ν_B (orange triangles). (e) Data for the Hahn echo delay sweep, where the inter-pule delay τ is swept simultaneously for both frequencies, showing comparable exponential decays.

do inherently multi-frequency measurements. We demonstrate the two-tone capabilities of our spectrometer with simultaneous Hahn echo delay sweeps at each frequency of our bimodal resonator, ν_A = 4024 MHz and ν_B = 4488 MHz; Figs. 6(a) and 6(b) show frequency sweep data for the two resonances. To make it easier to distinguish the signals at each frequency, we introduce a slight time offset for the pulses at ν_B, Δt_B = 200 ns, as shown in the pulse sequence schematic in Fig. 6(c). The pulse times for both frequencies are $t_{\pi/2} = t_\pi$ = 100 ns, and in this experiment we used the same delay times for both frequencies, though all such timings can be changed on a per-frequency basis. As discussed above, the sample used for this experiment, sample **B**, shows large enough inhomogeneous broadening such that we can detect echoes from a single sample at both frequencies at zero field. Background-subtracted echoes at a delay time of τ = 600 ns are shown in Fig. 6(d), and delay sweep data at each frequency are shown in (e), where in both cases the blue circles show the signal at ν_A and the orange triangles show the signal at ν_B. We see nearly identical exponential decays at each frequency, as we would expect for an inhomogeneously broadened sample. This result demonstrates the ability of the spectrometer to operate at two frequencies, separated by nearly 500 MHz, simultaneously.

IV. CONCLUSIONS

The spectrometer described herein is effective, flexible, and easy to assemble. In its current form it can perform many common ESR experiments and can be relatively easily extended to incorporate additional measurements in the future. With the appropriate choice of resonator, it enables experiments both within and outside the standard ESR frequency bands. Additionally, the multiple-output nature of the spectrometer enables two-tone ESR, where two different frequencies are sent to the resonator simultaneously. As demonstrated, the spectrometer itself currently supports such experiments, and our lab is working on refining the bimodal resonator design described above to allow simultaneous ESR for spin samples with frequencies separated by more than 1 GHz. With such a resonator, this spectrometer will allow us to measure and exploit the interaction between coupled spin systems with widely separated transition frequencies using double electron–electron resonance (DEER) experiments.

SUPPLEMENTARY MATERIAL

We provide the code used to program the FPGA, as well as the data acquisition code. Instrument drivers are provided for all equipment used, including the temperature controller/thermometer (Lakeshore 335) and programmable power supply (GPD-3303S). CAD files (in STL format) are provided for both LGRs.

ACKNOWLEDGMENTS

We acknowledge Jonathan Friedman, Brendan Sheehan, Kai-Isaak Ellers, and Andrew Mounce for useful conversations and advice, and Richard Winpenny for samples and useful conversations. The part of this work was enabled by the use of PyScan (github.com/sandialabs/pyscan), scientific measurement software made available by the Center for Integrated Nanotechnologies, an Office of Science User Facility operated for the U.S. Department of Energy. The support for this work was provided by the Hamilton College Dean of Faculty, the Muhlenberg College Provost, and the Muhlenberg College Dean of Students.

AUTHOR DECLARATIONS

Conflict of Interest

The authors have no conflicts to disclose.

Author Contributions

Charles A. Collett: Conceptualization (lead); Formal analysis (lead); Funding acquisition (lead); Investigation (lead); Methodology (lead); Resources (lead); Software (lead); Supervision (lead); Visualization (lead); Writing – original draft (lead); Writing – review & editing (lead). **Sofia M. Davvetas**: Investigation (supporting); Software (supporting); Writing – review & editing (supporting). **Abdulelah Alsuhaymi**: Resources (supporting); Writing – review & editing (supporting). **Grigore A. Timco**: Resources (supporting); Writing – review & editing (supporting).

DATA AVAILABILITY

The data that support the findings of this study are available from the corresponding author upon reasonable request.

APPENDIX A: SPECTROMETER COMPONENTS

Component	Part no.	Freq. Range (GHz)
RF source	WindFreakTech SynthHD	0.054–15
RF switch	MiniCircuits (MC) ZFSWA2R-63DR+	0.5–6
RF power divider	MC ZX10R-14-S+	0–10
Power amplifier	MC ZVA-183-S+	0.7–18
Digital step attenuator	MC ZX76-31R75PP-S+	0.009–6
Circulator	Fairview microwave (FM) SFC4080B/SFC2040A	4–8/2–4
RF limiter	MC VLM-63-2W-S+	0.03–6
Low-noise amplifier	FM SLNA-060-40-09-SMA	2–6
IQ mixer	Marki microwave MMIQ-0218LXPC	12–18
FPGA	Lattice ECP5 evaluation board	N/A

APPENDIX B: DIFFERENT FREQUENCY RANGES

Most of the original components work in the 2–6 GHz range, the main exception being the circulator; two circulators are provided above, for the 2–4 GHz range and the 4–8 GHz range. Accessing a higher frequency range (6–15 GHz) can be performed by substituting the following components (listed with component name and frequency range):

- RF switch: Analog devices HMC547ALP3 (evaluation board EV1HMC547ALP3), DC-20 GHz.
- RF Divider: This component can be removed, using output A as the mixer LO and output B as the pulsed output.
- Digital Step Attenuator: This component can be removed, and different tip angles achieved by varying the pulse width.
- RF Limiter: This component can be removed or replaced with an RF switch.
- Low-Noise Amplifier: Fairview Microwave FMAM1071, 6–18 GHz.
- Circulator: Fairview Microwave SFC0818, 8–18 GHz.

REFERENCES

[1]M. A. Nielsen and I. L. Chuang, *Quantum Computation and Quantum Information*, 10th ed. (Cambridge University Press, Cambridge, UK, 2010).
[2]D. Loss and D. P. DiVincenzo, Phys. Rev. A **57**, 120 (1998).
[3]A. Chiesa, P. Santini, E. Garlatti, F. Luis, and S. Carretta, Rep. Prog. Phys. **87**, 034501 (2024).
[4]A. Lund, M. Shiotani, and S. Shimada, *Principles and Applications of ESR Spectroscopy* (Springer Netherlands, Dordrecht, 2011).
[5]C. P. Poole, *Electron Spin Resonance: A Comprehensive Treatise on Experimental Techniques*, 2nd ed. (Wiley, New York, 1997).
[6]T. Kaufmann, T. J. Keller, J. M. Franck, R. P. Barnes, S. J. Glaser, J. M. Martinis, and S. Han, J. Magn. Reson. **235**, 95 (2013).
[7]J. E. McPeak, R. W. Quine, S. S. Eaton, and G. R. Eaton, Rev. Sci. Instrum. **90**, 024102 (2019).
[8]Z. Shi, S. Mu, X. Qin, Y. Dai, X. Rong, and J. Du, Rev. Sci. Instrum. **89**, 125104 (2018).
[9]Y. S. Yap, Y. Tabuchi, M. Negoro, A. Kagawa, and M. Kitagawa, Rev. Sci. Instrum. **86**, 063110 (2015).
[10]L. Stefanazzi, K. Treptow, N. Wilcer, C. Stoughton, C. Bradford, S. Uemura, S. Zorzetti, S. Montella, G. Cancelo, S. Sussman, A. Houck, S. Saxena, H. Arnaldi, A. Agrawal, H. Zhang, C. Ding, and D. I. Schuster, Rev. Sci. Instrum. **93**, 044709 (2022).
[11]C. Shannon, Proc. IRE **37**, 10 (1949).
[12]M. N. Leuenberger and D. Loss, Nature **410**, 789 (2001).
[13]J. R. Friedman and M. P. Sarachik, Annu. Rev. Condens. Matter Phys. **1**, 109 (2010).
[14]National Academies of Sciences, Engineering, and Medicine, *Advancing Chemistry and Quantum Information Science: An Assessment of Research Opportunities at the Interface of Chemistry and Quantum Information Science in the United States* (National Academies Press, Washington, DC, 2023).
[15]C. A. Collett, K.-I. Ellers, N. Russo, K. R. Kittilstved, G. A. Timco, R. E. P. Winpenny, and J. R. Friedman, Magnetochemistry **5**, 4 (2019).
[16]C. A. Collett, P. Santini, S. Carretta, and J. R. Friedman, Phys. Rev. Res. **2**, 032037 (2020).
[17]W. Froncisz and J. S. Hyde, J. Magn. Reson. **47**, 515 (1982).
[18]G. A. Rinard and G. R. Eaton, *Biomedical EPR, Part B: Methodology, Instrumentation, and Dynamics*, *Biological Magnetic Resonance No. 24/B*, edited by S. R. Eaton, G. R. Eaton, and L. J. Berliner (Kluwer Academic/Plenum Publishers, New York, 2005), pp. 19–52.
[19]E. R. Eisenach, J. F. Barry, L. M. Pham, R. G. Rojas, D. R. Englund, and D. A. Braje, Rev. Sci. Instrum. **89**, 094705 (2018).
[20]G. Joshi, J. Kubasek, I. Nikolov, B. Sheehan, T. A. Costa, R. A. Allão Cassaro, and J. R. Friedman, Rev. Sci. Instrum. **91**, 023104 (2020).
[21]F. K. Larsen, E. J. L. McInnes, H. E. Mkami, J. Overgaard, S. Piligkos, G. Rajaraman, E. Rentschler, A. A. Smith, G. M. Smith, V. Boote, M. Jennings, G. A. Timco, and R. E. P. Winpenny, Angew. Chem., Int. Ed. **42**, 101 (2003).
[22]S. Meiboom and D. Gill, Rev. Sci. Instrum. **29**, 688 (1958).
[23]G. Jeschke, in *ESR Spectroscopy in Membrane Biophysics, Biological Magnetic Resonance*, edited by M. A. Hemminga and L. J. Berliner (Springer US, Boston, MA, 2007), pp. 17–47.
[24]G. Timco, S. Marocchi, E. Garlatti, C. Barker, M. Albring, V. Bellini, F. Manghi, E. J. L. McInnes, R. G. Pritchard, F. Tuna, W. Wernsdorfer, G. Lorusso, G. Amoretti, S. Carretta, M. Affronte, and R. E. P. Winpenny, Dalton Trans. **45**, 016610 (2016).